Hemogenic and aortic endothelium arise from a common hemogenic angioblast precursor and are specified by the Etv2 dosage

Shizheng Zhao[a,1] 📶, Shachuan Feng[a,1] 📶, Ye Tian[a,1] 📶, and Zilong Wen[a,b,2] 📶

Hematopoietic stem cells (HSCs) are generated from hemogenic endothelial cells (HECs) in the floor of the dorsal aorta (DA) via endothelial-to-hematopoietic transition (EHT). Yet whether HECs and conventional endothelial cells (cECs) in the DA share a common precursor is controversial, and the molecular mechanisms governing their fate specification remain incompletely defined. Using a combination of fate mapping, time-lapse imaging, genetic manipulation, and single-cell RNA sequencing, here we show that HECs and cECs display strictly spatial separation in the DA where nearly all the endothelial cells in the floor and roof are HECs and cECs, respectively. We further show that HECs and cECs in the DA arise from a common hemogenic angioblast precursor, which differentiates into HECs and cECs during axial migration prior to the DA formation. The specification of HECs and cECs from hemogenic angioblasts is governed by the Etv2 dosage by differentially regulating Fli1a, Notch, and Sclβ. Finally, we document that pan-endothelial overexpression of transcriptional factor *runx1* is sufficient to promote HEC fate in the DA roof. Our study reveals the lineage origin of HECs and cECs in the DA and uncovers the molecular network controlling their fate specification.

endothelium | hemogenic endothelium | lineage origin | fate determination

During vertebrate embryogenesis, hematopoietic stem cells (HSCs) are generated from a subset of specialized endothelial cells (ECs), named hemogenic endothelial cells (HECs), via endothelial-to-hematopoietic transition (EHT) in the dorsal aorta (DA) (1–4). Time-lapse imaging and in situ analysis of hematopoietic markers indicate that HECs are located exclusively in the ventral domain/floor of the DA in the aorta-gonad-mesonephros (AGM), budding toward intraaortic lumen in avians (5, 6) and mice (2, 7, 8) or budding toward subaortic space between the DA and posterior cardinal vein in zebrafish (3, 4). Although HSC-forming HECs and non–blood-forming conventional endothelial cells (cECs) are both located in the DA, whether HECs and cECs arise from a common bipotent precursor remains debatable. Several studies using human pluripotent stem cells or murine model have suggested that HECs and cECs represent distinct lineages indicated by the expression of distinct cell surface markers, such as CD73 and CD184 (9), or by their different requirements of Notch signaling strengths (10). Studies in the avian model especially suggested that different mesoderm origins, somatopleural and splanchnic mesoderm, give rise to cECs and HECs, respectively (11, 12). In contrast to the distinct lineages model, other studies suggested a common precursor model that endothelial precursors appear to adopt arterial endothelial fate before committing into HECs (13, 14). Consistent with this model, recent single-cell RNA-sequencing (scRNA-seq) studies (15–17) constructed the continuous developmental trajectory from arterial cECs to HECs, showing that this transition is accompanied with gradual loss of arterial signatures and acquirement of hematopoietic features. To clarify this controversial issue, delicate in vivo fate mapping studies are required. In parallel, although multiple signaling pathways including Hedgehog, Wnt, Vegf, Notch, and BMP are reported critical for HEC and cEC fate specification (18–21), it seems that these signaling pathways eventually converge on the ECs-autonomous requirement of Notch signaling to activate key downstream transcriptional factors, including Gata2, Runx1, and Gfi1 (22–24). Besides, these key factors are also regulated by the upstream factors, including Etv2 and Scl (25–27). Precisely how these upstream factors interplay with Notch signaling and form a genetic network to control cEC and HEC fate specification remains unexplored.

Zebrafish is a prominent model for studying many aspects of developmental biology including angiogenesis and hematopoiesis (28, 29). In zebrafish, the first wave of endothelial progenitors, named angioblasts, in the trunk region arises from the posterior lateral

Significance

Hematopoietic stem cells (HSCs) are generated from specialized endothelial cells, called hemogenic endothelial cells (HECs). It has been debated whether HECs and non–HSC-forming conventional endothelial cells (cECs) arise from a common precursor or represent distinct lineages. Moreover, the molecular basis underlying their distinct fate determination is poorly understood. We use photoconvertible labeling, time-lapse imaging, and single-cell RNA-sequencing analysis to trace the lineage of HECs. We discovered that HECs and cECs arise from a common hemogenic angioblast precursor, and their distinct fate is determined by high or low dosage of Etv2, respectively. Our results illuminate the lineage origin and a mechanism on the fate determination of HECs, which may enhance the understanding on the ontogeny of HECs in vertebrates.

[1]S.Z., S.F., and Y.T. contributed equally to this work.

[2]To whom correspondence may be addressed. Email: zilong@ust.hk.

plate mesoderm at ~11 h postfertilization (hpf), migrates toward the midline during 14 to 18 hpf, and finally coalesces to form the DA at 21 hpf (30, 31). Similar to mammals, HECs in zebrafish are located in the floor of the DA and express several early hematopoiesis-related genes, including *gata2b*, *sclβ*, and *runx1* (13, 23, 26). During 30 to 60 hpf, HECs undergo EHT and directly bud from the floor of the DA toward the subaortic space (3, 4). Because of the unique advantages of in vivo imaging and genetic amenability, the zebrafish model system provides a powerful tool to dissect the lineage origin of HECs and cECs and the mechanism controlling their fate specification.

In this report, we combined in vivo photoconversion lineage tracing, time-lapse imaging, and scRNA-seq analysis to study the ontogeny of HECs and cECs. We showed that the ventral and dorsal endothelia of the zebrafish DA are largely HECs and cECs, respectively. We further documented that HECs and cECs arise from a common precursor, termed hemogenic angioblast, which undergoes HEC and cEC fate specification prior to the DA formation. Genetic studies further unraveled that at early stage, high and low dosages of Etv2 determine HEC and cEC fates through differentially regulating the expression and activity of *fli1a*, *sclβ*, and Notch. Finally, we showed that ectopic expression of transcription factor Runx1 in the roof of the DA can convert cECs into HECs.

Results

The Endothelia in the Floor of the DA Are HECs. To have a better understanding of the ontogeny of HECs and cECs, we generated a double transgenic line *Tg(flk1:eGFP;flk1:NLS-Eos)*, in which all ECs in the DA express enhanced green fluorescent protein (eGFP) in the cytoplasm and photoconvertible Eos protein in the nucleus (32). This transgenic line allows us to label ECs in the roof or the floor of the DA and follow their behavior by time-lapse imaging (Fig. 1A) during EHT from 28 to 72 hpf (3, 4). We photoconverted 5 to 10 ECs per embryo in the DA floor at 26 hpf and immediately tracked their behavior by time-lapse imaging until 72 hpf (Fig. 1B). Unexpectedly, we found that ~96% (211 out of 220) of the photoconverted floor ECs underwent EHT (Fig. 1D), of which ~49% (104 out of 211) of the cells underwent EHT directly, ~45% (96 out of 211) of the cells divided at least once before initiating EHT, and ~5% (11 out of 211) of the cells burst into pieces, a phenotype similar to abortive EHT observed in *runx1* knockdown embryos (3, 26) (Fig. 1C). Whether the abortive EHT is a natural phenomenon or a consequence of experimental artifacts is unclear. Nonetheless, these data indicate that ~96% of the ECs in DA floor undergo EHT, and most of them eventually become hematopoietic stem/progenitor cells (HSPCs). Since there are only ~34 cells in the DA floor at
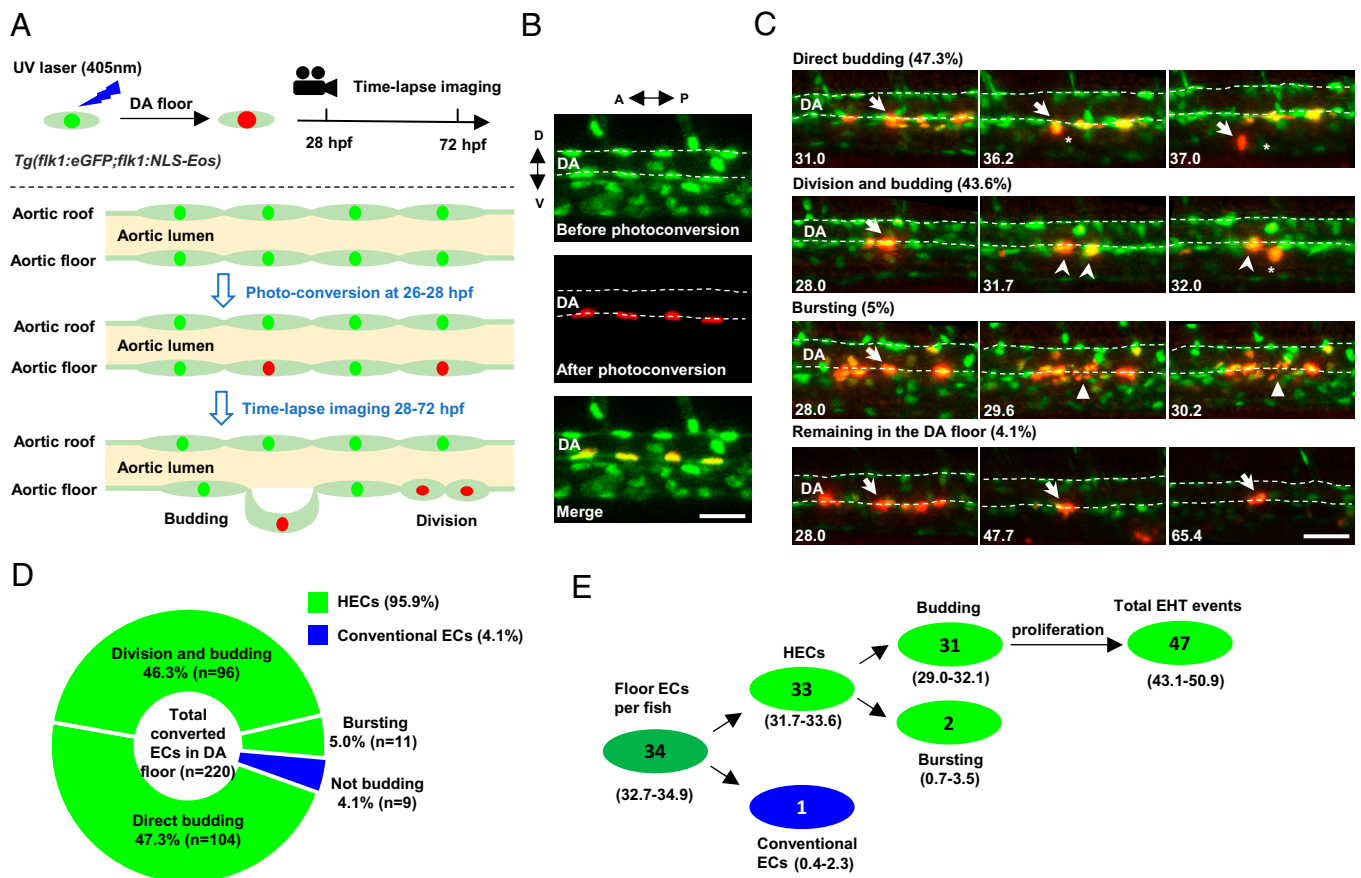

Fig. 1. Time-lapse imaging indicates that the endothelium in the DA floor are HECs. (A) Schematic diagram showing the strategy of photoconversion of the floor endothelium in the DA and time-lapse imaging in *Tg(flk1:eGFP;flk1:NLS-Eos)* transgenic zebrafish. The green, red, and light green dots indicate the nuclei before photoconversion, the nuclei after photoconversion, and eGFP in the cytoplasm, respectively. (B) Representative images of the photoconverted floor endothelium at 26 hpf. (C) Images representing four types of behaviors of the DA floor endothelium during EHT (28 to 72 hpf) captured by time-lapse imaging. The dashed lines indicate the roof and floor boundaries of the DA, the white arrow indicates successfully converted cells, the white arrowhead indicates the descendants of labeled cells, the white triangle indicates bursting cells, and the asterisk indicates budding cells. Captured time points are labeled at the bottom left. (D) Summary of the behaviors of floor endothelium during 28 to 72 hpf captured by time-lapse imaging. (E) Estimated number of HECs and cECs in the DA floor per fish and their behaviors with 95% (CI). Data were analyzed with 220 cells by five independent experiments with 40 embryos. A, anterior; D, dorsal; P, posterior; V, ventral. (Scale bars, 30 μm.)

27 hpf per embryo, this result predicts that 33 of them are HECs, and only 1 cell is cEC (Fig. 1*E*). Considering that ECs are patterned around the DA circumference unevenly (31), we believe that the rare cECs which we observed in the DA floor in our photoconversion assay might result from the mislabeling of the lateral ECs of the DA. Based on these findings, we conclude that nearly all the ECs in the DA floor at around 26 to 28 hpf are HECs.

The Endothelium in the DA Roof Are cECs Lacking Hemogenic Potential. In avian and mammalian embryos, HECs are reported to undergo EHT toward the DA lumen to form intraaortic hematopoietic clusters (IAHCs) (2, 5, 33, 34). These IAHCs are not only restricted to the floor but also observed in the DA roof of murine embryos (7, 33, 35). However, whether these IAHCs in the DA roof are generated in situ or arise from the floor remains elusive. Owing to the advantages of time-lapse imaging and high resolution of ECs labeling, the *Tg(flk1:eGFP;flk1:NLS-Eos)* fish provides a useful tool to address this issue. Therefore, we photoconverted the ECs in the DA roof at 26 hpf and monitored their behaviors (Fig. 2*A*). Time-lapse imaging showed that, while the majority (∼67%; $n = 103/154$; fish = 21) of the ECs remained in the DA roof/lateral during 28 to 72 hpf, a substantial portion (∼33%; $n = 51/154$; fish = 21) of the ECs moved ventrally and repositioned to the floor of the DA, some of which underwent cell division before and during the ventral movement (Fig. 2 *B* and *C*). Remarkably, the ventral movement of the roof ECs appeared to be temporally correlated with the EHT in the floor (Fig. 2*D*), indicating that the loss of HECs due to EHT in the DA floor is largely replenished by the ventral movement of roof ECs, which is consistent with the previous observation (3, 36, 37). However, direct budding of ECs from the DA roof was never observed, although two EHT events (∼1%; $n = 2/154$; fish = 21) were captured after the roof ECs moved ventrally and repositioned to the floor (Fig. 2*C*). Given that there are ∼35 ECs in the DA roof at 27 hpf per embryo, this result means that less than 1 cell from the DA roof undergoes EHT per embryo (Fig. 2*E*). Taken together, these data demonstrate that the ECs in the DA roof are all cECs lacking hemogenic potential.

HECs and cECs Arise from a Common Precursor and Separate prior to the DA Lumen Formation. To delineate the mechanism governing the fate determination of HECs and cECs, we isolated single ECs from the DA roof and the floor respectively using the *Tg(flk1:eGFP;flk1:NLS-Eos)* zebrafish after photoconversion and then performed scRNA sequencing (Fig. 3*A*). These single ECs were isolated at two different time points, 21 and 28 hpf, when the lumen of the DA is established (31) and the EHT begins (3, 4), respectively. Uniform manifold approximation and projection (UMAP) clustering analysis identified two clusters, Cluster_roof and Cluster_floor, enriched in the ECs from the roof and floor, respectively (Fig. 3*A* and *SI Appendix*, Fig. S1*A*). Differentially expressed gene and gene ontology (GO) analyses showed that the feature genes, including *flk1*, *cdh5*, *tbx20*, *sox18*, *efnb2a*, *hey2*, and *dll4*, enriched in roof ECs (Fig. 3*B*) were associated with vasculogenesis, angiogenesis, and vessel development (*SI Appendix*, Fig. S1*B*), showing the vascular identity of these cells. In contrast, the enriched GO terms of floor ECs were associated with catabolic and metabolic processes (*SI Appendix*, Fig. S1*B*) and were highly enriched in HEC markers and definitive hematopoiesis-related genes, such as *gfi1aa*, *scl*, *myb*, *dnmt3ba*, *ikzf1*, *gata2b*, and *runx1* (Fig. 3*B*), showing that they are in an active metabolic state with hematopoietic potential. These data indicate that Cluster_roof and Cluster_floor represent cECs and HECs, respectively, and that their fates have already been separated by 21 hpf. To
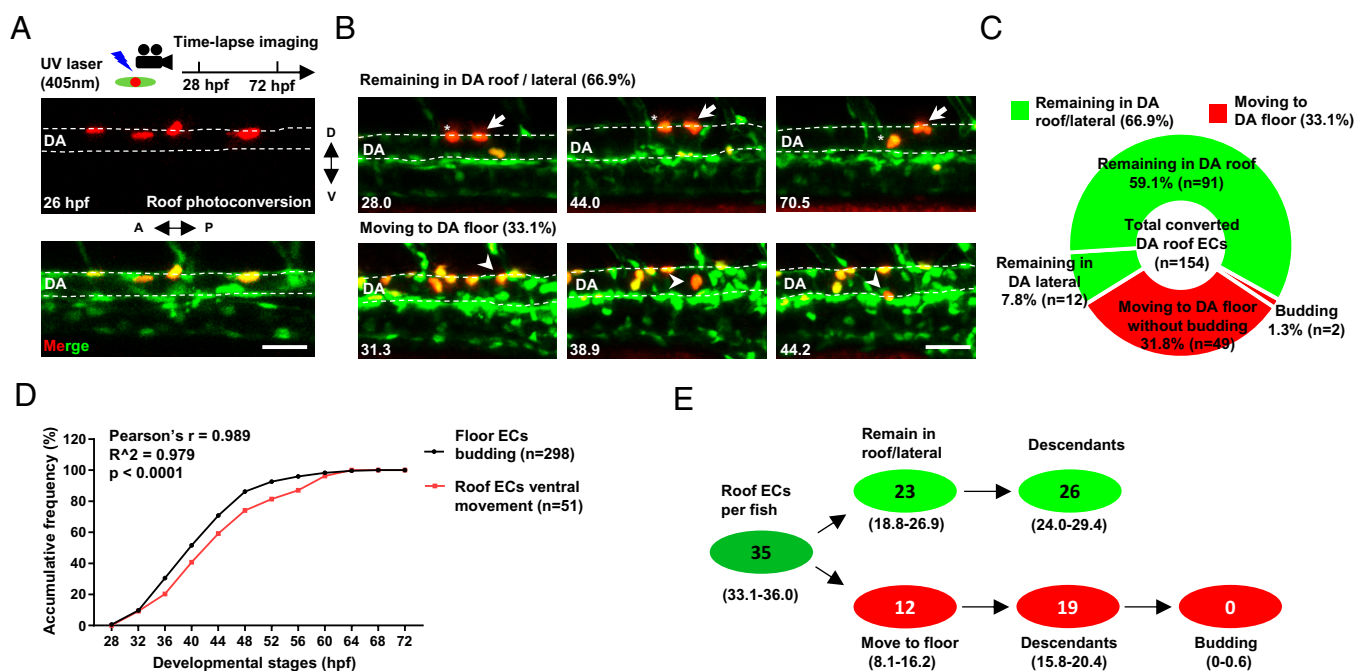

Fig. 2. Time-lapse imaging reveals that the endothelium in the DA roof are cECs. (*A*) Schematic diagram showing the strategy of photoconversion in the DA roof endothelium and time-lapse imaging in *Tg(flk1:eGFP;flk1:NLS-Eos)* transgenic zebrafish. (*B*) Images representing two types of behaviors of the DA roof endothelium during 28 to 72 hpf captured by time-lapse imaging. The dashed line indicates the roof and floor boundary of the DA, the white arrow indicates cells remaining in the DA roof, the asterisk indicates cells remaining in the DA lateral, and the white arrowhead indicates cells moving to the DA floor. Captured time points are labeled at the bottom left. (*C*) Summary of the behaviors of the DA roof endothelium during 28 to 72 hpf captured by time-lapse imaging. (*D*) Line graph showing the accumulative frequency percentage (%) of the floor ECs budding ($n = 298$) and the roof ECs ventral movement ($n = 51$) during 28 to 72 hpf. Pearson correlation coefficient r was calculated according to the frequency distribution. (*E*) Estimated number of HECs and cECs in the DA roof per fish and their behaviors with 95% (CI). Data were analyzed with 154 cells by four independent experiments with 21 embryos. (Scale bars, 30 μm.)
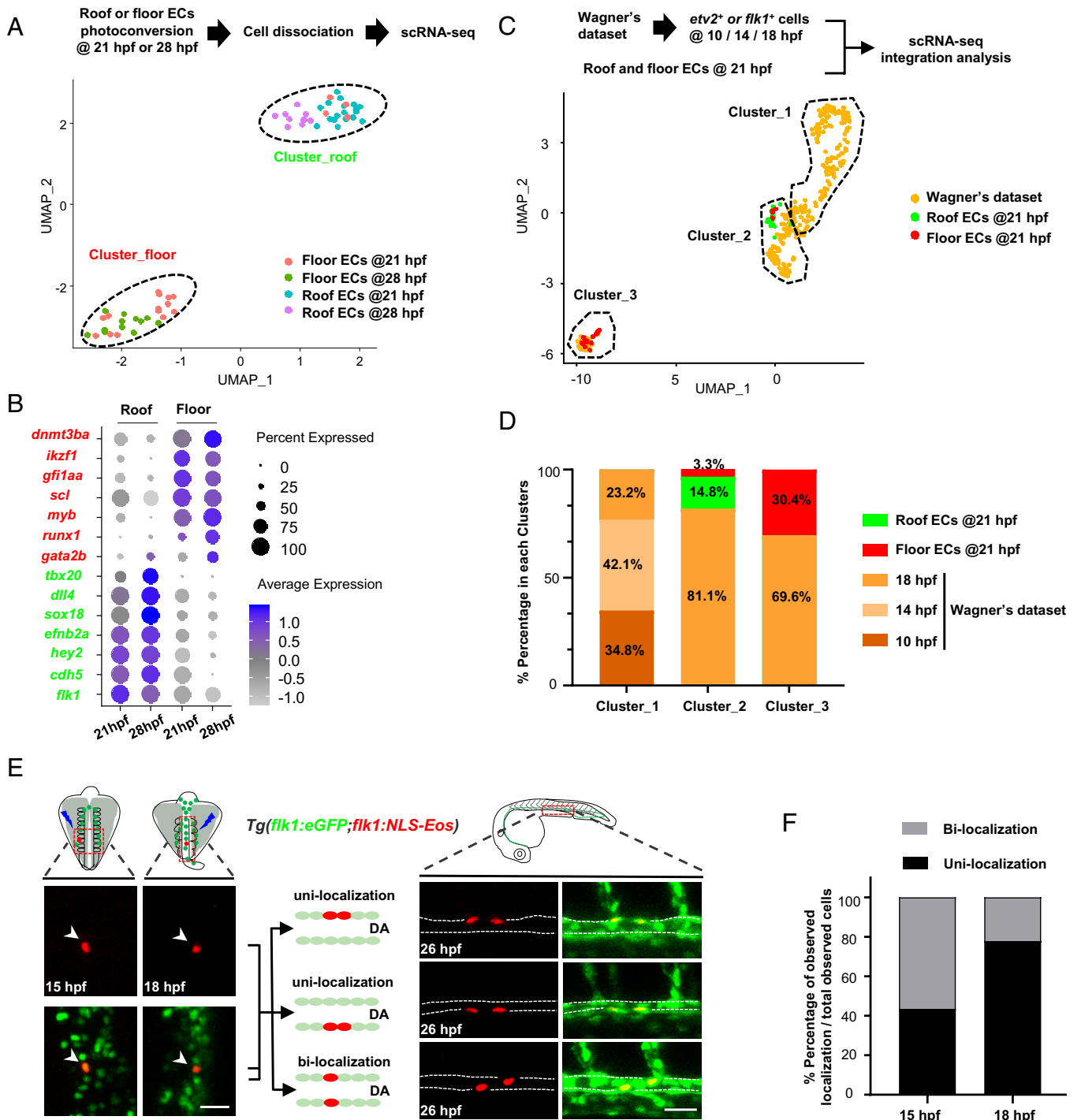
Fig. 3. scRNA-seq and fate mapping analyses reveal that HECs and cECs arise from a common precursor and separate prior to the DA formation. (*A*) Isolation of single ECs from the DA roof or floor after photoconversion (21 hpf, roof/floor ECs, *n* = 18/18; 28 hpf, roof/floor ECs, *n* = 10/12) and UMAP plot for cell clustering analysis. (*B*) Dot plot showing representative marker genes expression enriched in the roof and floor ECs at 21 and 28 hpf. (*C*) UMAP plot of cell clustering analysis of integrated dataset (Wagner's dataset at 10, 14, and 18 hpf and dataset at 21 hpf in this study). (*D*) Distribution percentage (%) of the cells from different time points in each cluster. (*E*) Single-cell photoconversion and fate mapping analysis in *Tg(flk1:eGFP;flk1:NLS-Eos)*. (*Left*) Representative images showing single Eos+ cells photoconverted at 15 and 18 hpf. (*Upper Left*) Photoconverted areas (see details in *Materials and Methods*). (*Right*) Three different localization patterns at 26 hpf (roof and floor only or both in the DA) of the descendants (≥ 2) derived from a single converted Eos+ cell. (*Upper Right*) The observed DA region (see details in *Materials and Methods*). (*F*) Bar plot shows the percentage (%) of unilocalization and bilocalization cells in total converted cells at 15 hpf (number of cells: total *n* = 24; unilocalization *n* = 11; bilocalization *n* = 13) and 18 hpf (number of cells: total *n* = 45; unilocalization *n* = 35; bilocalization *n* = 10) stages. Data were acquired by two independent experiments (*A*) or analyzed by three independent photoconversion experiments (*E* and *F*). Cell numbers equal to embryo numbers for single-cell lineage tracing in *F*. (Scale bars, 30 μm.)

further define the time window during which HECs and cECs are specified, we reanalyzed the Wagner's scRNA-seq database from early developmental stages of zebrafish embryos (38) at 10-, 14-, and 18-hpf stages. By integration analysis with our single-cell RNA-seq dataset (21-hpf stage), we found that the 21-hpf cells from our dataset were predominantly (33/36; ∼92%) clustered with mesoderm cells defined in Wagner's study (38) (*SI Appendix*, Fig. S1*C*). To gain insights into these clusters,

we further extracted the information of *etv2⁺* or *flk1⁺* cells, which presumably include HECs, cECs, and their precursors, angioblasts (30, 39), from 10-, 14-, and 18-hpf stages. We then integrated the extracted *etv2⁺* and *flk1⁺* scRNA-seq dataset (referred to as Wagner's dataset in Fig. 3*C*) with our scRNA-seq dataset (21-hpf stage) and reperformed clustering analysis. UMAP results identified three clusters, Cluster_1, Cluster_2, and Cluster_3 (Fig. 3*C* and *SI Appendix*, Fig. S2*A*). We found that the roof ECs and floor ECs from the 21-hpf embryos were predominantly clustered in Cluster_2 and Cluster_3, respectively (Fig. 3*C*), suggesting that Cluster_2 and Cluster_3 represent ECs which have already committed to cEC and HEC lineage, while Cluster_1 likely represents noncommitted precursors. Indeed, this notion was further supported by the findings that the Cluster_1 contained a high percentage of *etv2* single positive cells with feature genes involved in early developmental process, e.g., embryonic organ morphogenesis and anterior/posterior pattern specification (*SI Appendix*, Fig. S2 *B–D*). Moreover, the cEC marker *dll4* and HEC marker *gata2b* were highly expressed in Cluster_2 and Cluster_3, respectively, but absent in Cluster_1 (*SI Appendix*, Fig. S2*E*). Next, we examined the distribution percentage of the three clusters at different time points of zebrafish development. The results showed that Cluster_1 consists of cells from 10-, 14-, and 18-hpf stages exclusively, whereas Cluster_2 and Cluster_3 consist of cells predominantly from 18- and 21-hpf stages, with a small fraction of cells from 14 hpf (∼0.8%) in Cluster_2 (Fig. 3*D*), suggesting that cECs and HECs in the DA are likely to arise from a common angioblast precursor, and their fates are largely determined during the period of 14 to 18 hpf, which correlates with the time window when somite-derived Notch signals were shown to specify HEC formation (40, 41).

To further support our hypothesis, we performed single-cell fate mapping analysis using the *Tg(flk1:eGFP;flk1:NLS-Eos)* zebrafish. In this assay, we photoconverted a single *flk1-Eos⁺* cell in each embryo at 15 or 18 hpf and defined the identity of the photoconverted cell by examining the distribution pattern of its progenies (if the converted single cell produced two or more progenies) in the DA roof and floor at 26 hpf (Fig. 3*E*). We reasoned that if cECs and HECs indeed originated from a common precursor and their fates were specified between 14 and 18 hpf, we would expect to observe two different distribution patterns, bilocalization and unilocalization. The bilocalization indicates successful labeling of a common precursor capable of giving rise to both cECs and HECs, whereas the unilocalization indicates successful labeling of a lineage committed cell capable of giving rise to either cECs or HECs (Fig. 3*E*). In agreement with our hypothesis, single-cell fate mapping revealed that ∼55.5 and ∼44.5% of the cells displayed bilocalization and unilocalization potential at the 15-hpf stage, respectively (Fig. 3*F*). As fish developed to the 18-hpf stage, the percentage of the cells with bilocalization potential dropped to ∼22.2%, accompanied by an increase of the percentage (∼77.8%) of the cells with unilocalization potential (Fig. 3*F*), indicating a gradual fate commitment process from bipotent progenitors to unipotent lineage-committed cells during this developmental time window. These results, together with the scRNA-seq data analysis, demonstrate that cECs and HECs in the DA indeed originate from a common *flk1⁺* precursor, which we refer to as hemogenic angioblast, and their fates are largely determined during the period of 14 to 18 hpf, well before the lumen formation of the DA.

Etv2 Dosage Determines HEC and cEC Fate through Differentially Regulating the Activities of Fli1a, Notch, and Scl β. Having defined the lineage origin of HECs and cECs, we next investigated

the mechanism controlling their fate specification. The Ets variant 2 (*etv2*) has been identified as a master regulator for HEC and cEC development (25, 42), yet the underlying mechanism remains incompletely clear. To dissect the role of Etv2 in HEC and cEC development, we generated a transgenic fish *Tg(etv2:NLS-d2eGFP)*, in which a fast-degraded d2eGFP protein is under control of the *etv2* promoter (43) (*SI Appendix*, Fig. S3*A*), and performed fluorescence-activated cell sorting (FACS) analysis at 16 hpf, when HECs and cECs are known to be specified (Fig. 3 *C*, *D*, and *F*). Intriguingly, two *etv2⁺* cell fractions, *etv2*-d2eGFP^high and *etv2*-d2eGFP^low, were detected (Fig. 4*A*). qPCR analysis showed that the expression of the HEC marker, *gata2b* (23), was significantly enriched in *etv2*-d2eGFP^high fraction (Fig. 4*A*). This observation prompted us to hypothesize that Etv2 dosage might govern the fate choice between HECs and cECs. To test this hypothesis, we generated a double transgenic line *Tg(etv2:mCherry-T2a-CreER^{T2};flk1:loxP-DsRedx-loxP-eGFP)* (*SI Appendix*, Fig. S3*A*) and performed lineage tracing analysis by pulsing embryos with a range of 4-Hydroxytamoxifen (4-OHT) doses between 15 and 17 hpf when HECs and cECs are undergoing fate specification (Fig. 4*B*). The resulting *flk1*-GFP⁺ cells were examined at 32 hpf, which is the latest timing point used in the study to address the presence and localization of HECs in the aortic floor. Results showed that low (2.5 µM) and median (5 µM) dose treatment produced limited numbers of GFP⁺ cells exhibiting bias distribution pattern toward the floor of the DA (Fig. 4*B*). On the other hand, high-dose (15 µM) treatment led to a significant increase of GFP⁺ cells displaying comparable number in the floor and roof (Fig. 4*B*). In parallel, we also tested different lengths of time (1, 1.5, and 2 h) of 4-OHT treatment with median dose (5 µM). Results showed that three groups exhibited labeling bias toward floor of the DA, but the bias toward floor was decreased in the group of 2-h treatment (*SI Appendix*, Fig. S3*B*). These data suggest that the progenitors with high and low Etv2 dosages preferentially adopt the HEC and cEC fates, respectively. To further support this notion, we generated another transgenic line *Tg(hsp70l:etv2-P2a-mCherry)*, in which Etv2-P2a-mCherry protein is under control of the *hsp70l* promoter (*SI Appendix*, Fig. S3*A*), and asked whether overexpression of Etv2 during 14 to 18 hpf would enhance HEC formation. Indeed, whole-mount in situ hybridization (WISH) showed a robust increase of *gata2b* and *runx1* expression in the DA (Fig. 4*C*), suggesting that high Etv2 dosage promotes HEC fate. Consistent with the overexpression results, injection of low-dose *etv2* MO (25, 42) into fertilized embryos at the one-cell stage (*SI Appendix*, Fig. S3*C*) dramatically reduced *gata2b* and *runx1* expression in the DA (Fig. 4*C*), showing that reduced *etv2* expression blocks HEC formation. Notably, the DA formation remained intact in both Etv2 overexpression and low-dose *etv2* MO knockdown embryos (Fig. 4*C*), indicating that low Etv2 dosage is sufficient for cEC specification. Collectively, these data indicate that *etv2* expression level, high and low dosage, determines HEC and cEC fate specification from hemogenic angioblasts, respectively.

Previous studies have documented that the *etv2-fli1a* axis is sufficient for cEC specification (25, 44) (*SI Appendix*, Fig. S4*A*). Consistent with this notion, *fli1a* expression was detected, although at a lower level, in low-dose *etv2* MO knockdown embryos (*SI Appendix*, Fig. S4*B*), which explained the intact vascular structure in low-dose *etv2* MO knockdown embryos (Fig. 4*C*). Yet the mechanism controlling the HEC specification is less clear. To dissect the genetic network governing HEC fate specification behind Etv2 high dosage, we monitored the Notch signaling, which has been shown as a key regulator in
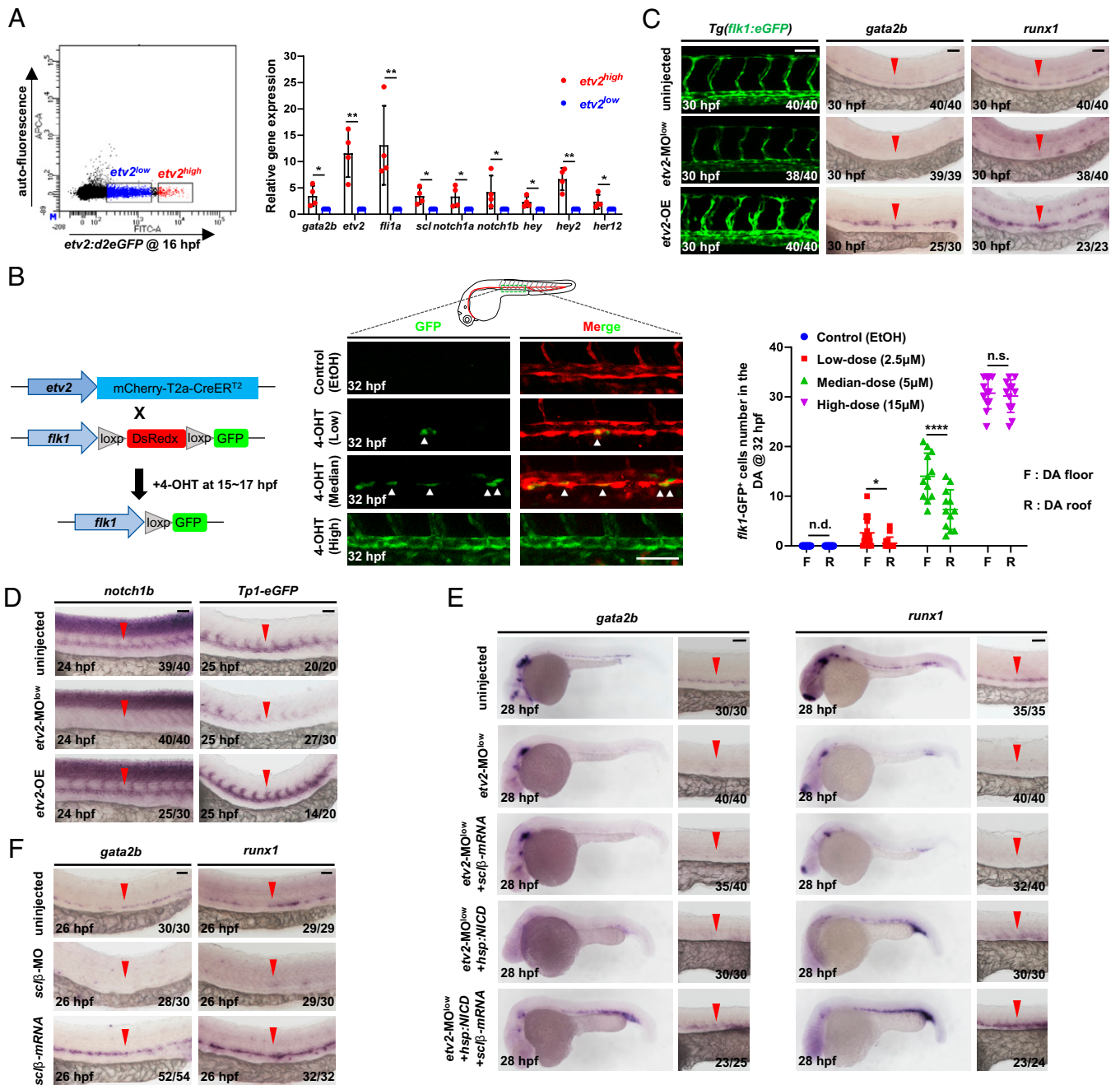
Fig. 4. Etv2 dosage determines HEC and cEC fate through differentially regulating the activities of Fli1a, Notch, and Sclβ. (*A*) Flow cytometric and gene expression analysis of *Tg(etv2:d2eGFP)* embryos. Representative results of flow cytometric analysis at 16 hpf and relative genes expression levels in the *etv2*-d2eGFP*high* and *etv2*-d2eGFP*low* population. (*B*) Strategy to perform lineage tracing using double transgenic line *Tg(etv2:mCherry-T2a-CreER^{T2} ;flk1:loxp-DsRedx-loxp-eGFP)*. Fish were treated with EtOH or different doses of 4-OHT during 15 to 17 hpf, and GFP$^+$ ECs were quantified at 32 hpf. (*C*) Lateral views of the DA in *Tg(flk1:eGFP)* embryos and WISH of *gata2b* and *runx1* in embryos. The embryos were injected with or without a low dose of *etv2* MO (*etv2-MO^{low}*) to knockdown *etv2* or heat-shocked to overexpress *etv2* (*etv2-OE*). (*D*) WISH of *notch1b* and *eGFP*. The embryos were injected with or without a low dose of *etv2* MO to knockdown *etv2* or heat-shocked to overexpress *etv2*. (*E*) WISH of *gata2b* and *runx1* indicates rescue of HECs. The embryos were uninjected or injected with a low dose of *etv2* MO, together with or without overexpressing *sclβ* (mRNA injection) and NICD (heat shock) alone or both. (*F*) WISH of *gata2b* and *runx1* in *sclβ* MO knockdown and *sclβ* overexpression embryos. The embryos were injected with or without *sclβ* MO or *sclβ* mRNA. Data are representative of two independent experiments (four biological replicates in *A*; for embryos, *n* = 12 in *B*) or two different clutches of embryos (*C*–*F*). n/N reports the number of embryos with staining pattern in image/total embryos (*C*–*F*). Heat shock was performed at 14 hpf for 45 min in *C*–*E*. Student's *t* tests were used in *A*; two-way ANOVA test was used in *B*. Data are represented as mean ± SD, *$P \leq 0.05$, **$P \leq 0.01$, ****$P \leq 0.0001$; n.s., not significant ($P > 0.05$); n.d., not detectable. (Scale bars, 60 μm.)

HEC fate determination (20, 45). We found that the expressions of *notch1* receptors (*notch1a/notch1b*) and Notch downstream targets (*hey/hey2/her12*) were significantly enriched in the *etv2*-d2eGFP*high* cell fraction (Fig. 4*A*), suggesting that high Etv2 dosage may function through regulating Notch activity. To test this possibility, we examined the expression of *notch* receptors and Notch activity under *etv2* overexpression and low-dose *etv2* MO

knockdown conditions. Results showed that the expressions of arterial *notch* receptors (*notch1a/notch1b/notch3*) (46), Notch downstream targets (*hey/hey2/her12*), and *Tp1-eGFP* reporter in the DA were significantly enhanced in *etv2* overexpression embryos and dramatically reduced in low-dose *etv2* MO knockdown embryos (Fig. 4*D* and *SI Appendix*, Fig. S4 *C* and *D*). In contrast, *etv2* expression, as indicated by the formation of the bilateral stripes

of *etv2*^{+} cells, was largely unaffected in Delta-Notch signaling-deficient *mib* mutants (47) (*SI Appendix*, Fig. S4E), indicating that Etv2 regulates HEC specification, at least in part, through modulating Notch activity. Notably, *fli1a* expression was also highly enriched in *etv2*-d2eGFP^{high} population (Fig. 4A), which is consistent with previous findings that *fli1a* is a downstream target of Etv2 (44), suggesting that Fli1a may be involved in the HEC specification. Indeed, we showed that injection of *fli1a* messenger RNA (mRNA) into low-dose *etv2* MO knockdown embryos could partially rescue the expression of *Tp1*-eGFP reporter (*SI Appendix*, Fig. S4C), suggesting that Notch signaling is regulated directly by Etv2 as well as indirectly through Fli1a. We therefore wondered whether restoration of Notch signaling is sufficient to rescue HEC formation in low-dose *etv2* MO knockdown embryos, in which *fli1a* was expressed at low level (*SI Appendix*, Fig. S4B) by overexpressing Notch intracellular domain (NICD), the dominant activator of Notch pathway. Results showed that NICD overexpression only marginally rescued HECs (Fig. 4E), suggesting that additional downstream factor(s) are required for HEC specification. We then turned to *sclβ*, an *etv2* downstream target which has been shown indispensable for *runx1* expression in the DA (25, 26). We found that overexpressing Sclβ together with NICD, but not Sclβ or NICD alone, robustly rescued the HEC formation (Fig. 4E), suggesting that Sclβ and Notch are two key Etv2 downstream targets which act in parallel and collaboratively to activate *gata2b-runx1* axis for HEC specification. Indeed, epistatic analysis showed that Sclβ and Notch were independent of each other as indicated by the normal expression of *sclβ* and *Tp1*-eGFP reporter in *mib* mutants and *sclβ* morphants (48), respectively (*SI Appendix*, Fig. S4 E and F). Consistent with this notion, *gata2b* and *runx1* expression were diminished in *sclβ* MO knockdown embryos and overexpressing *sclβ* drastically enhanced *gata2b* and *runx1* expression (Fig. 4F), placing *sclβ* upstream of the *gata2b-runx1* axis. Taken together, these data demonstrate that the fate commitment of cECs and HECs from hemogenic angioblasts is determined by the Etv2 dosage, in which low dosage of Etv2 triggers low levels of Fli1a and Notch to direct cEC formation (25), whereas high dosage of Etv2 induces high levels of Fli1a, Notch, and Sclβ expression, leading to the promotion of HEC specification (*SI Appendix*, Fig. S5).

Runx1 Overexpression Promotes HEC Fate in the Roof of the DA. Our above analysis placed the activation of the *gata2b-runx1* axis as the final effector for HEC specification. Yet whether induction of *gata2b-runx1* expression is sufficient to promote HEC formation in vivo remains unclear. To address this issue, we generated a transgenic line *Tg(flk1:runx1-P2a-GFP)*, in which Runx1-P2a-GFP expression was under control of the pan-endothelial *flk1* promoter (31) (Fig. 5A), and asked whether ectopically expressing *runx1* in the DA roof endothelium could promote the HEC formation. To facilitate our analysis, we outcrossed the *Tg(flk1:runx1-P2a-GFP)* line with the *Tg(flk1:NLS-Eos)* fish. The resulting double transgenic fish *Tg(flk1:runx1-P2a-GFP;flk1:NLS-Eos)* enabled us to label the ECs in the DA roof at 26 to 28 hpf and followed their behavior by time-lapse imaging. Consistent with previous results (Fig. 2C), only 3 out of 352 roof ECs (3/352, ~0.85%) underwent EHT in control siblings (Tg⁻; *n* = 32) (Fig. 5 B and C). Strikingly, in *runx1* overexpression embryos (Tg⁺; *n* = 40), 57 out of 408 roof ECs analyzed underwent EHT, a 17-fold increase compared to control siblings (~14% versus ~0.85%) (Fig. 5C). We further showed that the DA roof-born Eos⁺ HECs were able to colonize the caudal hematopoietic tissue (CHT) and thymus after EHT (Fig. 5 D and E), suggesting that the roof-born HECs in *runx1* overexpression fish are indeed

capable of becoming hematopoietic cells. This conclusion was further supported by the findings that the *Tg(flk1:runx1-P2a-GFP)* fish produced significantly more *myb*⁺ HSPCs than control siblings (Fig. 5 F and G). Taken together, these results demonstrate that *runx1* overexpression is sufficient for the conversion, at least in part, of HECs' fate in the DA roof. Interestingly, we noticed that all 57 EHT events from the DA roof in *runx1* overexpression embryos took place after they had moved ventrally and repositioned in the floor of the DA (Fig. 5D), supporting the notion that EHT occurs exclusively in the floor of the DA.

Discussion

In this study, we reported a systematic investigation on the ontogeny of cECs and HECs from early lineage fate mapping, genetic fate determination, and spatial distribution in the DA. By combining photoconversion with time-lapse imaging, we unexpectedly found that nearly the entire aortic floor endothelium are HECs, whose loss during EHT is replenished by the ventral movement and proliferation of the roof cECs in the DA. Interestingly, our above finding is similar to the previous study in the avian model that the aortic floor appears to be a transitory structure and would be completely replaced by roof and side ECs in the aorta (11), suggesting that a similar model would also be utilized in mammals.

Our study here provides in vivo evidence that cECs and HECs in the DA arise from a bipotent common progenitor, which undergoes fate separation during the time window of 14 to 18 hpf, and finally colonize the DA roof and floor accordingly. This common progenitor, as shown in our fate mapping data, is in a previously defined *flk1*⁺ angioblasts population (30, 31) and distinct from the previous conception, hemangioblasts, which refer to preprimitive wave mesodermal cells giving rise to yolk sac blood islands in mouse (49) and primitive erythrocytes and ECs in zebrafish (50). We therefore term the common precursors of cECs and HECs as hemogenic angioblasts, which represent a branch point between definitive hemogenic endothelium and conventional endothelium in the DA. Notably, our common progenitor model appears different from the previous findings in avians, which showed that distinct mesoderm regions, the somatopleural and the splanchnopleural mesoderm, give rise to aortic roof and floor endothelium, respectively (6, 11, 12, 51). The discrepancy between the avian and zebrafish models might be explained by the different methods used in the two model systems. Instead of the single-cell resolution photoconversion assay performed here, the transplantation assay employed in avian model is mainly based on anatomical recognition with lower resolution. Hence, the transplantation assay may not reflect the endogenous developmental trajectory of aortic roof and floor endothelium. Alternatively, the discrepancy is attributed to the species difference between avian and fish. Notably, several studies have suggested that, like zebrafish, the ontogeny of the DA in mice appears to arise from single mesodermal source (52, 53), implying that mammals may employ a mechanism similar to that of zebrafish.

Another interesting observation in our study is that ectopic *runx1* overexpression can promote HEC formation in the roof of the DA, and yet these roof-derived *runx1* overexpressing cells undergo EHT only after they have repositioned to the floor of the DA. This observation indicates that in addition to the early fate determination during the time window of 14 to 18 hpf, extrinsic signals are required for the induction of EHT. One possible mechanism is that the floor niche produces extrinsic induction signals to trigger the initiation of EHT. Alternatively, the roof environment generates extrinsic inhibitory signals to
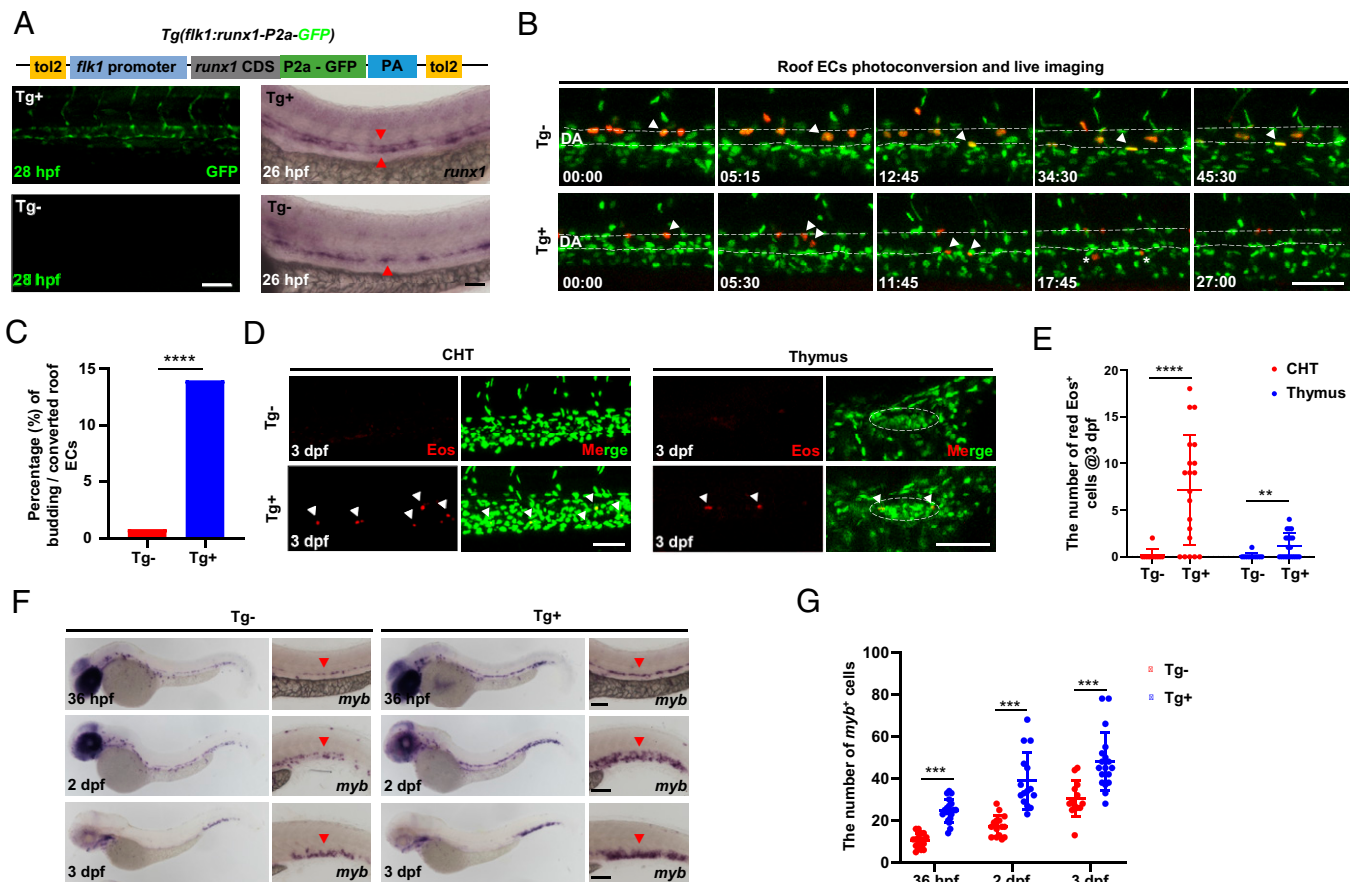
Fig. 5. Runx1 overexpression promotes HEC fate in the DA roof. (*A*) Schematic graph showing the construction of *Tg(flk1:runx1-P2a-GFP)* with representative confocal images of stable F1 fish at 28 hpf and *runx1* WISH at 26 hpf. (*B*) Representative behaviors of the photoconverted DA roof ECs captured by time-lapse imaging during 28 to 72 hpf in Tg$^+$ (*runx1* overexpression) and Tg$^-$ (siblings without *runx1* expression) embryos. The dashed lines denote the roof and floor walls of the DA, the triangles denote converted cells, and the asterisks denote budding cells. (*C*) Quantification of percentage (%) of the budding roof ECs divided by the photoconverted roof ECs (3/352 in Tg$^-$ versus 57/408 in Tg$^+$). (*D*) Representative confocal images (after Z-projection) in CHT and thymus at 3 dpf. Fifteen DA roof ECs were photoconverted at 26 hpf in each Tg$^+$ or Tg$^-$ embryo, and red Eos$^+$ cells were quantified at 3 dpf. The dashed circles denote the location of thymus. (*E*) Quantification of red Eos$^+$ cells in CHT and thymus at 3 dpf. (*F*) WISH of *myb* in Tg$^+$ and Tg$^-$ embryos. (*G*) Quantification of *myb$^+$* cells. Data are representative of three independent experiments with 32 (Tg$^-$) and 40 (Tg$^+$) embryos in *B* and *C* or two different clutches of embryos with (36 hpf, Tg$^-$ /Tg$^+$: *n* = 18/19; 2dpf, Tg$^-$ /Tg$^+$: *n* = 15/15; 3dpf, Tg$^-$ /Tg$^+$: *n* = 15/18) for *myb* WISH (*F* and *G*) or 11 (Tg$^-$) and 20 (Tg$^+$) embryos for photoconversion and quantification (*D* and *E*). Fisher's exact test was used in *C*, unpaired Student's *t* tests were used in *E* and *G*. **$P \leq 0.01$, ***$P \leq 0.001$, ****$P \leq 0.0001$. (Scale bars, 60 μm.)

prevent EHT in the roof of the DA. It is unclear which mechanism is correct, and perhaps both mechanisms are involved. Indeed, recent studies in zebrafish have broadened the understanding of the EHT process by showing that mechanical force generated by blood flow plays a critical role in controlling the ventral emergence and EHT budding direction of the HECs (36, 37). Notably, a previous study, in which the authors utilized the whole-mount transparency method to quantify all hematopoietic clusters (c-Kit$^+$) temporally and spatially in E10.5 murine embryos, observed that some c-Kit$^+$ clusters were distributed along the dorsal wall of the DA in E10.5 murine embryos, while most of the c-Kit$^+$ clusters were ventrally localized (35). However, the whole-mount transparency method could not provide direct evidence supporting that the c-Kit$^+$ clusters along the dorsal wall indeed arise in situ. It will be of interest to reinvestigate whether the dorsal wall of the murine DA consists of HECs. Finally, according to our data, we speculate that Runx1 expression does not seem to regulate the movements of the roof cells from the roof to the floor, since cell movements from the roof to the floor occur regardless of whether the roof cells express Runx1 or not, as indicated in *runx1*-overexpression or wild-type embryos, respectively. Instead, Runx1 is likely to play a role in HEC formation and EHT process (24, 54, 55).

Finally, we have proposed a model in which the Etv2 dosage plays a critical role in cEC and HEC fate specification (*SI Appendix*, Fig. S5). Previous studies identified that *Fli1* (42, 44), *Scl* (25, 42), *Notch1* (27), and *Dll4* (56) are downstream of *Etv2* in the regulation of EC development. Our study further reveals that low Etv2 dosage is sufficient to promote cEC commitment by inducing a low level of Fli1a, whereas high Etv2 dosage induces HEC lineage commitment through inducing a higher level of Fli1a and Sclβ expression and higher activity of Notch signaling. Interestingly, we also retrieved the scRNA-seq gene expression matrix of four cell populations (Conflux AE, pre-HE, HE, and IAC) from a murine scRNA-seq dataset reported previously (17) and examined the expression of *Etv2*, *Scl*, *Notch*, *Gata2*, and *Runx1*. We observed an increase of both *Etv2* expression level and the percentage of *Etv2*-positive cells between pre-HE and HE populations, accompanied with the increase of *Runx1* expression (*SI Appendix*, Fig. S6 *A–D*). Likewise, the expression levels and positive cell proportions are also increased for *Scl*, *Notch2*, and *Notch3* but not for *Gata2* (*SI Appendix*, Fig. S6 *D* and *E*), which seems to be constitutively highly expressed in those four populations. The discrepancy of the *Gata2* expression between zebrafish and murine datasets may be due to species difference since zebrafish contain duplicated *gata2a*

and *gata2b* genes, and only *gata2b* shows HEC-specific expression (23). Nevertheless, the overall expression of the key transcriptional regulators seems to be highly conserved between these two datasets, suggesting a similar mechanism may be applied to the murine model. It will be of great interest to further investigate this issue in the murine model. Another interesting finding is that our epistatic analysis indicates Sclβ act upstream of *gata2b* and is required for *gata2b* expression in a Notch-independent manner. However, how Sclβ regulates *gata2b* expression remains unknown. Given the fact that the enhancers of *Gata2*, *Fli1*, and *Scl* are shown to be active during murine HSC ontogeny (57) and they have also been shown to form a recursively wired gene-regulatory circuit during early mouse hematopoietic development (58), we speculate that Sclβ may act collaboratively with Fli1a to regulate *gata2b* expression in zebrafish. Further studies will be required to clarify these issues.

Materials and Methods

Zebrafish Strains. Zebrafish were maintained according to standard protocols (59). Zebrafish were kept at 28.5 °C in a 14-h light and 10-h dark cycle. After natural spawning, embryos were collected and raised at 28.5 °C in 0.5 × E2 medium containing methylene blue (egg water). To avoid pigmentation, embryos were changed to 0.003% *N*-Phenylthiourea (P7629, Sigma) in egg water at 1 dpf. The following strains were used: *Tg(flk1: eGFP)*^{s843} (31), *Tg(flk1:NLS-Eos)*^{ncv6} (32), *Tg(Tp1:eGFP)*^{um14} (60), *Tg(hsp70l: NICD-eGFP)* (61), *Tg(fli1:DsRed)*^{um13} (62), *Tg(flk1:loxP-DsRedx-loxP-eGFP)* (63), *mib*^{ta52b} (64), *Tg(etv2:NLS-d2eGFP)hkz*037, *Tg(hsp70l:etv2-P2a-mCherry)hkz*038, *Tg(etv2:mCherry-T2a-CreER*^{T2} *)hkz*039, *Tg(flk1:loxP-DsRedx-loxP-eGFP)hkz*040, and *Tg(flk1:runx1-P2a-GFP)hkz*041. All animal experiments were conducted according to the guidelines of the Animal and Plant Care Facility and approved by the Animal Ethics Committee of the Hong Kong University of Science and Technology.

Generation of Transgenic Lines. The destabilized d2eGFP with nuclear localization sequence (NLS-d2eGFP) and mCherry-T2a-CreER^{T2} sequence were placed under the c2 *etv2* promoter (43). Zebrafish full-length coding sequence of *etv2* gene plus *P2a-mCherry* was cloned under *hsp70l* promoter (65). Zebrafish full-length coding sequence of *runx1* gene plus *P2a-GFP* was cloned under ~6.5 kb *flk1* promoter (31). The above sequences were inserted into the modified pBluescript II SK(+) vector containing two arms of Tol2 sequences. The resulting *etv2:NLS-d2eGFP*, *etv2:mCherry-T2a-CreER*^{T2}, *hsp70l:etv2-P2a-mCherry*, and *flk1:runx1-P2a-GFP* constructs were then injected into one-cell–stage embryos with transposase mRNA. The injected embryos were raised to adulthood for germline transmission screening.

Photoconversion Fate Mapping, Time-Lapse Imaging, Image Processing, and Unilocalization/Bilocalization Identification. For early fate mapping analysis, a single *flk1*-Eos$^+$ cell of *Tg(flk1:eGFP;flk1:NLS-Eos)* was converted by 405-nm UV laser at 15- and 18-hpf stages in each embryo as described (66). Single EC was randomly photoconverted within the 8- to 13-somite region at 15 hpf or 6- to 18-somite region at 18 hpf. With exception of three embryos, all photoconverted ECs could give rise to ECs of the DA in the AGM region (8- to 17-somite region) at 26 hpf (pretested in this study). For time-lapse imaging to capture EHT, the ECs (5 to 10 cells) in the DA of *Tg(flk1:eGFP;flk1:NLS-Eos)* embryos were converted by 405-nm UV laser at around 26 hpf. The embryos were subsequently mounted in 1% low–melting-point agarose in E3 embryo medium with 0.01% tricaine for anesthetization as described (66). Time-lapse imaging was carried out on SP8 confocal microscope using a 20× dry objective (Leica). A heated microscope chamber at 28.5 °C was used for recording time-lapse videos. Stacks were taken every 15 min with a step size of 3.0 to 5.0 μm. Confocal stacks and time-lapse videos were analyzed using ImageJ (NIH). For unilocalization/bilocalization identification of descendant cells, Z projections of images were first performed. The roof/floor (cEC/HEC) ECs were identified according to the same criterion (0 to 45° from the dorsal–ventral axis of the DA) relative to the roof/floor boundary indicated by the *flk1*-eGFP expression (37).

Heat Shock, Morpholino Injection, and mRNA Injection. Morpholinos were purchased from Gene-Tools (USA) and dissolved in distilled water. One ng/nL (high dose) or 0.1 ng/nL (low dose) of *etv2* MO (42) was injected into one-cell–stage embryos. The high dose of *etv2* MO completely blocked the *etv2*-d2eGFP expression of the *Tg(etv2:NLS-d2eGFP)* reporter (*SI Appendix*, Fig. S3C), while the low dose of *etv2* MO (≤ 0.3 ng/nL) partially reduced *etv2*-d2eGFP expression (*SI Appendix*, Fig. S3C). *scl*β MO knockdown was performed as previously described (26), and 8 ng of *scl*β MO was injected into one-cell–stage embryos. The mRNA of *fli1a* and *scl*β were synthesized by using mMessage mMachine Kit (Ambion Inc.). The primers for amplifying *fli1a* and *scl*β full-length coding sequences and injected dosage of *fli1a* (60 pg) and *scl*β (200 pg) mRNA were referenced to a previous report (25). For heat shock experiments, embryos at the 10-somite stage (14 hpf) were collected in a 50-mL Falcon tube containing 5 mL of E3 embryo medium and submerged in a 40 °C water bath for 45 min.

WISH, Double Fluorescence In Situ Hybridization, and Immunofluorescent Antibody Staining. WISH was performed as described (66). AP-conjugated anti-DIG antibody (11093274910; Roche) and BM purple (11442074001; Roche) were used as the substrate for color reaction. Double fluorescence in situ hybridization (dFISH) assay was performed as described (67). POD-conjugated anti-fluorescein antibody (11426346910; Roche), POD-conjugated anti-digoxigenin antibody (11207733910; Roche), and TSA-Cy3 or TSA-FITC (NEL741001KT; PerkinElmer) were used for color reaction. The RNA probes were in vitro synthesized with T7 RNA polymerase (Promega) with dig-RNA-labeling mix (11277073910; Roche) or fluorescein-RNA-labeling mix (11685619910; Roche). The probes sequences are listed below: runx1 (NM_131603.3; 385–2069), gata2b (NM_001002689.1; 809–1669), notch1b (NM_131302.2; 4757–6080), etv2 (NM_001037375.1; 65–1165), fli1a (NM_131348.2; 104–1459), scl (NM_213237.1; 518–1138), and eGFP (eGFP full-length coding sequence). For antibody staining, the pretreatment of embryos was similar to WISH as described above. Anti-cleaved caspase3 (559565, Biosciences, diluted at 1:500) and Alexa 555-anti-rabbit antibody (A31572, Invitrogen, diluted at 1:400) were used as primary and secondary antibody, respectively. WISH images were captured by Stereo Discovery V20 microscope (Zeiss) with digital camera (DS-Ri2, Nikon). dFISH and antibody staining images were captured by SP8 confocal microscope (Leica) and analyzed by ImageJ (NIH).

FACS, cDNA Synthesis, and qPCR. The embryos at desired stages were pooled together (each biological replicate with 60 to 100 embryos) and homogenized by syringe with 27G needle. The cell suspension was prepared as previously described (68) and subjected to FACS analysis (FACS Aria IIIu). The cDNA was prepared from sorted cells (100 to 500 cells per well; two or four technical replicates per biological sample) and amplified by Smart-seq2 protocol (69). Real-time qPCR was performed to quantify the transcripts of *gata2b*, *etv2*, *fli1a*, *scl*, *notch1a*, *notch1b*, *notch3*, *hey*, *hey2*, and *her12*. Primers for qPCR used in this work are listed in *SI Appendix*, Table S1.

Single-Cell Isolation, cDNA Preparation, and RNA-seq. For single-cell isolation, 10 to 20 cells in the DA roof or floor of each *Tg(flk1:eGFP;flk1:NLS-Eos)* embryo were photoconverted at 21 or 28 hpf under a confocal microscope. Thirty embryos were anesthetized, and the trunk regions containing the converted cells were dissected with 27G needle in ice-cold phosphate-buffered saline (PBS). The dissected tissues were dissociated into single-cell suspension according to the protocol (70). After 20 min digestion, the single-cell suspension was pushed through a 40-μm Cell Strainer (352340, BD Falcon) and transferred to the 35-mm petri dish (150460, Invitrogen). A single red Eos$^+$ cell was collected manually with the micromanipulator system (NT-88-V3, Nikon) under a fluorescence microscope (Nikon), then washed by transferring the cell to a drop of 500 μL RNase-free PBS with 2% bovine serum albumin, and finally transferred into RNase-free 200 μL tube (Eppendorf) containing 4.4 μL lysis buffer (69). The yield and efficiency of manual single-cell collection were relatively low. In our hand, we were able to collect 20 to 30 single RNA-qualified cells from 300 to 600 photoconverted cells within 2 h after digestion. The Smart-seq2 protocol (69) was used for whole-transcriptome amplification, and the cDNA library was prepared as previously described (68). Library quality

was assessed using the Agilent Fragment Analyzer System, and the samples were sent to Novogene Company Limited for Illumina Hiseq X Ten 150-bp paired-end sequencing with an average depth of 6×10^6 raw reads per sample.

Bioinformatic Analysis of RNA-seq. Reads were aligned to the GRCz11.94 zebrafish reference genome using Spliced Transcripts Alignment to a Reference aligner (2.7.1a). Aligned reads were converted to counts for each gene using featureCounts (Rsubread_2.6.1). Dataset from 21- and 28-hpf roof cECs and floor HECs were analyzed by Seurat package (v.4.0.2). Cell quality control was performed before analysis based on minimal detected genes (default, $n = 200$). First, variable genes (default, $n = 2,000$) were identified based on variance stabilizing transformation using a normalized matrix. Principal component analysis was then performed (Dims = 1:20) followed by scaling scRNA-seq data. Finally, a plot graph was constructed by shared nearest neighbor–based clusters of the subtypes and transformed to UMAP for dimension reduction for intuitive visualization. The top 100 maker genes were identified based on spatial information (roof versus floor). GO analysis was performed with the clusterProfiler package (v.3.16.1) using the top 100 marker genes. For RNA-seq data integration analysis, GSE112294 (38) was reanalyzed by fetching counts data at 10, 14, and 18 hpf. Because etv2 expression decreases as endothelial precursors undergo differentiation, we set criteria as etv2 expression (counts > 0) at 10 and 14 hpf, flk1 expression (counts > 0) at 18 hpf, to extract potential endothelial/precursor cells, referred to as "Wagner's dataset." The Wagner's dataset was integrated with the 21-hpf dataset by the FindIntegrationAnchors function implanted in the Seurat package. Following the standard integration analysis tutorial (https://satijalab.org/seurat/articles/integration_introduction.html), we set DefaultAssay as "integrated" and performed clustering analysis. All the analysis was performed in the R (version 4.0.2) environment.

Quantification and Statistical Analysis. Statistical parameters including the exact value of n are reported in Figs. 1, 2, 4, and 5 and the figure legends of Figs. 1–5. All statistical analyses were performed using GraphPad-Prism version 8. Paired or unpaired Student's t tests were used to calculate the two-tailed P value for comparisons, clarified in the figure legends of Figs. 4 and 5. Data were presented as mean $\pm$ SD. Statistical significance is shown as follows: ns, $P > 0.05$; *$P \leq 0.05$; **$P \leq 0.01$; ***$P \leq 0.001$; and ****$P \leq 0.0001$.

Author affiliations: [a]Division of Life Science, State Key Laboratory of Molecular Neuroscience, Center of Systems Biology and Human Health, Hong Kong University of Science and Technology, Clear Water Bay, Kowloon, Hong Kong 999077, China; and [b]Greater Bay Biomedical Innocenter, Shenzhen Bay Laboratory, Shenzhen Peking University, Hong Kong University of Science and Technology Medical Center, Shenzhen 518055, China

1. H. M. Eilken, S. Nishikawa, T. Schroeder, Continuous single-cell imaging of blood generation from haemogenic endothelium. Nature **457**, 896–900 (2009).
2. J. C. Boisset et al., In vivo imaging of haematopoietic cells emerging from the mouse aortic endothelium. Nature **464**, 116–120 (2010).
3. K. Kissa, P. Herbomel, Blood stem cells emerge from aortic endothelium by a novel type of cell transition. Nature **464**, 112–115 (2010).
4. J. Y. Bertrand et al., Haematopoietic stem cells derive directly from aortic endothelium during development. Nature **464**, 108–111 (2010).
5. L. Pardanaud, F. Dieterlen-Lièvre, Emergence of endothelial and hemopoietic cells in the avian embryo. Anat. Embryol. (Berl.) **187**, 107–114 (1993).
6. T. Jaffredo, R. Gautier, A. Eichmann, F. Dieterlen-Lièvre, Intraaortic hemopoietic cells are derived from endothelial cells during ontogeny. Development **125**, 4575–4583 (1998).
7. C. Mizuochi et al., Intra-aortic clusters undergo endothelial to hematopoietic phenotypic transition during early embryogenesis. PLoS One **7**, e35763 (2012).
8. M. Tavian et al., Aorta-associated CD34+ hematopoietic cells in the early human embryo. Blood **87**, 67–72 (1996).
9. A. Ditadi et al., Human definitive haemogenic endothelium and arterial vascular endothelium represent distinct lineages. Nat. Cell Biol. **17**, 580–591 (2015).
10. L. Gama-Norton et al., Notch signal strength controls cell fate in the haemogenic endothelium. Nat. Commun. **6**, 8510 (2015).
11. C. Pouget, R. Gautier, M. A. Teillet, T. Jaffredo, Somite-derived cells replace ventral aortic hemangioblasts and provide aortic smooth muscle cells of the trunk. Development **133**, 1013–1022 (2006).
12. L. Pardanaud et al., Two distinct endothelial lineages in ontogeny, one of them related to hemopoiesis. Development **122**, 1363–1371 (1996).
13. F. Bonkhofer et al., Blood stem cell-forming haemogenic endothelium in zebrafish derives from arterial endothelium. Nat. Commun. **10**, 3577 (2019).
14. G. I. Uenishi et al., NOTCH signaling specifies arterial-type definitive hemogenic endothelium from human pluripotent stem cells. Nat. Commun. **9**, 1828 (2018).
15. Y. Zeng et al., Tracing the first hematopoietic stem cell generation in human embryo by single-cell RNA sequencing. Cell Res. **29**, 881–894 (2019).
16. S. Hou et al., Embryonic endothelial evolution towards first hematopoietic stem cells revealed by single-cell transcriptomic and functional analyses. Cell Res. **30**, 376–392 (2020).
17. Q. Zhu et al., Developmental trajectory of prehematopoietic stem cell formation from endothelium. Blood **136**, 845–856 (2020).
18. R. N. Wilkinson et al., Hedgehog and Bmp polarize hematopoietic stem cell emergence in the zebrafish dorsal aorta. Dev. Cell **16**, 909–916 (2009).
19. Y. Wei et al., Ncor2 is required for hematopoietic stem cell emergence by inhibiting Fos signaling in zebrafish. Blood **124**, 1578–1585 (2014).
20. K. Kumano et al., Notch1 but not Notch2 is essential for generating hematopoietic stem cells from endothelial cells. Immunity **18**, 699–711 (2003).
21. W. K. Clements et al., A somitic Wnt16/Notch pathway specifies haematopoietic stem cells. Nature **474**, 220–224 (2011).
22. M. G. Daniel, K. Rapp, C. Schaniel, K. A. Moore, Induction of developmental hematopoiesis mediated by transcription factors and the hematopoietic microenvironment. Ann. N. Y. Acad. Sci. **1466**, 59–72 (2020).
23. E. Butko et al., Gata2b is a restricted early regulator of hemogenic endothelium in the zebrafish embryo. Development **142**, 1050–1061 (2015).
24. A. D. Yzaguirre, E. D. Howell, Y. Li, Z. Liu, N. A. Speck, Runx1 is sufficient for blood cell formation from non-hemogenic endothelial cells in vivo only during early embryogenesis. Development **145**, dev158162 (2018).
25. X. Ren, G. A. Gomez, B. Zhang, S. Lin, Scl isoforms act downstream of etsrp to specify angioblasts and definitive hematopoietic stem cells. Blood **115**, 5338–5346 (2010).
26. F. Zhen, Y. Lan, B. Yan, W. Zhang, Z. Wen, Hemogenic endothelium specification and hematopoietic stem cell maintenance employ distinct Scl isoforms. Development **140**, 3977–3985 (2013).
27. F. Liu et al., Induction of hematopoietic and endothelial cell program orchestrated by ETS transcription factor ER71/ETV2. EMBO Rep. **16**, 654–669 (2015).
28. M. N. Chávez, G. Aedo, F. A. Fierro, M. L. Allende, J. T. Egaña, Zebrafish as an emerging model organism to study angiogenesis in development and regeneration. Front. Physiol. **7**, 56 (2016).
29. J. L. O. de Jong, L. I. Zon, Use of the zebrafish system to study primitive and definitive hematopoiesis. Annu. Rev. Genet. **39**, 481–501 (2005).
30. V. Kohli, J. A. Schumacher, S. P. Desai, K. Rehn, S. Sumanas, Arterial and venous progenitors of the major axial vessels originate at distinct locations. Dev. Cell **25**, 196–206 (2013).
31. S. W. Jin, D. Beis, T. Mitchell, J. N. Chen, D. Y. Stainier, Cellular and molecular analyses of vascular tube and lumen formation in zebrafish. Development **132**, 5199–5209 (2005).
32. S. Fukuhara et al., Visualizing the cell-cycle progression of endothelial cells in zebrafish. Dev. Biol. **393**, 10–23 (2014).
33. S. Taoudi, A. Medvinsky, Functional identification of the hematopoietic stem cell niche in the ventral domain of the embryonic dorsal aorta. Proc. Natl. Acad. Sci. U.S.A. **104**, 9399–9403 (2007).
34. M. F. T. R. de Bruijn, N. A. Speck, M. C. E. Peeters, E. Dzierzak, Definitive hematopoietic stem cells first develop within the major arterial regions of the mouse embryo. EMBO J. **19**, 2465–2474 (2000).
35. T. Yokomizo, E. Dzierzak, Three-dimensional cartography of hematopoietic clusters in the vasculature of whole mouse embryos. Development **137**, 3651–3661 (2010).
36. P. Campinho, P. Lamperti, F. Boselli, A. Vilfan, J. Vermot, Blood flow limits endothelial cell extrusion in the zebrafish dorsal aorta. Cell Rep. **31**, 107505 (2020).
37. M. Lancino et al., Anisotropic organization of circumferential actomyosin characterizes hematopoietic stem cells emergence in the zebrafish. eLife **7**, e37355 (2018).
38. D. E. Wagner et al., Single-cell mapping of gene expression landscapes and lineage in the zebrafish embryo. Science **360**, 981–987 (2018).
39. B. Chestnut, S. Sumanas, Zebrafish etv2 knock-in line labels vascular endothelial and blood progenitor cells. Dev. Dyn. **249**, 245–261 (2020).
40. I. Kobayashi et al., Jam1a-Jam2a interactions regulate haematopoietic stem cell fate through Notch signalling. Nature **512**, 319–323 (2014).
41. S. S. Rho et al., Rap1b promotes notch-signal-mediated hematopoietic stem cell development by enhancing integrin-mediated cell adhesion. Dev. Cell **49**, 681–696.e6 (2019).
42. S. Sumanas, S. Lin, Ets1-related protein is a key regulator of vasculogenesis in zebrafish. PLoS Biol. **4**, e10 (2006).
43. M. O. Schupp, M. Waas, C. Z. Chun, R. Ramchandran, Transcriptional inhibition of etv2 expression is essential for embryonic cardiac development. Dev. Biol. **393**, 71–83 (2014).
44. M. J. Abedin et al., Fli1 acts downstream of Etv2 to govern cell survival and vascular homeostasis via positive autoregulation. Circ. Res. **114**, 1690–1699 (2014).
45. L. T. Krebs et al., Notch signaling is essential for vascular morphogenesis in mice. Genes Dev. **14**, 1343–1352 (2000).
46. A. D. Kim et al., Discrete Notch signaling requirements in the specification of hematopoietic stem cells. EMBO J. **33**, 2363–2373 (2014).
47. M. Itoh et al., Mind bomb is a ubiquitin ligase that is essential for efficient activation of Notch signaling by Delta. Dev. Cell **4**, 67–82 (2003).

48. F. Qian *et al.*, Distinct functions for different scl isoforms in zebrafish primitive and definitive hematopoiesis. *PLoS Biol.* **5**, e132 (2007).

49. T. L. Huber, V. Kouskoff, H. J. Fehling, J. Palis, G. Keller, Haemangioblast commitment is initiated in the primitive streak of the mouse embryo. *Nature* **432**, 625–630 (2004).

50. K. M. Vogeli, S. W. Jin, G. R. Martin, D. Y. Stainier, A common progenitor for haematopoietic and endothelial lineages in the zebrafish gastrula. *Nature* **443**, 337–339 (2006).

51. T. Jaffredo *et al.*, Aortic remodelling during hemogenesis: Is the chicken paradigm unique? *Int. J. Dev. Biol.* **54**, 1045–1054 (2010).

52. Y. Tanaka *et al.*, Circulation-independent differentiation pathway from extraembryonic mesoderm toward hematopoietic stem cells via hemogenic angioblasts. *Cell Rep.* **8**, 31–39 (2014).

53. Y. Tanaka *et al.*, Early ontogenic origin of the hematopoietic stem cell lineage. *Proc. Natl. Acad. Sci. U.S.A.* **109**, 4515–4520 (2012).

54. C. Lancrin *et al.*, GFI1 and GFI1B control the loss of endothelial identity of hemogenic endothelium during hematopoietic commitment. *Blood* **120**, 314–322 (2012).

55. M. Lie-A-Ling *et al.*, Regulation of RUNX1 dosage is crucial for efficient blood formation from hemogenic endothelium. *Development* **145**, dev149419 (2018).

56. J. D. Wythe *et al.*, ETS factors regulate Vegf-dependent arterial specification. *Dev. Cell* **26**, 45–58 (2013).

57. P. Gao *et al.*, Transcriptional regulatory network controlling the ontogeny of hematopoietic stem cells. *Genes Dev.* **34**, 950–964 (2020).

58. J. E. Pimanda *et al.*, Gata2, Fli1, and Scl form a recursively wired gene-regulatory circuit during early hematopoietic development. *Proc. Natl. Acad. Sci. U.S.A.* **104**, 17692–17697 (2007).

59. M. Westerfield, *The Zebrafish Book: A Guide for the Laboratory Use of Zebrafish (Danio Rerio)* (University of Oregon Press, 2000).

60. M. J. Parsons *et al.*, Notch-responsive cells initiate the secondary transition in larval zebrafish pancreas. *Mech. Dev.* **126**, 898–912 (2009).

61. C. Zhang *et al.*, m^{6}A modulates haematopoietic stem and progenitor cell specification. *Nature* **549**, 273–276 (2017).

62. J. A. Villefranc, J. Amigo, N. D. Lawson, Gateway compatible vectors for analysis of gene function in the zebrafish. *Dev. Dyn.* **236**, 3077–3087 (2007).

63. S. He *et al.*, In vivo single-cell lineage tracing in zebrafish using high-resolution infrared laser-mediated gene induction microscopy. *eLife* **9**, e52024 (2020).

64. Y. J. Jiang *et al.*, Mutations affecting neurogenesis and brain morphology in the zebrafish, Danio rerio. *Development* **123**, 205–216 (1996).

65. M. C. Halloran *et al.*, Laser-induced gene expression in specific cells of transgenic zebrafish. *Development* **127**, 1953–1960 (2000).

66. Y. Tian *et al.*, The first wave of T lymphopoiesis in zebrafish arises from aorta endothelium independent of hematopoietic stem cells. *J. Exp. Med.* **214**, 3347–3360 (2017).

67. G. Lauter, I. Söll, G. Hauptmann, Two-color fluorescent in situ hybridization in the embryonic zebrafish brain using differential detection systems. *BMC Dev. Biol.* **11**, 43 (2011).

68. S. Wu *et al.*, Two phenotypically and functionally distinct microglial populations in adult zebrafish. *Sci. Adv.* **6**, eabd1160 (2020).

69. S. Picelli *et al.*, Full-length RNA-seq from single cells using Smart-seq2. *Nat. Protoc.* **9**, 171–181 (2014).

70. L. A. Samsa, N. Fleming, S. Magness, L. Qian, J. Liu, Isolation and characterization of single cells from zebrafish embryos. *J. Vis. Exp.* **109**), 53877 (2016).